

Efficient reduction of stellar contamination and noise in planetary transmission spectra using neural networks (unabridged)

David S. Duque-Castaño^{1, *}, Lauren Flor-Torres¹, and Jorge I. Zuluaga¹

SEAP/FACOM, Instituto de Física - FCEN, Universidad de Antioquia, Calle 70 No. 52-21, Medellín, Colombia

Received January XX, 2026; In original form January XX, 2026

ABSTRACT

Context. The characterization of exoplanetary atmospheres has been transformed by the James Webb Space Telescope (JWST), whose infrared sensitivity enables transmission spectroscopy at unprecedented precision. However, stellar heterogeneities (e.g., spots and faculae) remain a dominant source of contamination that can bias atmospheric retrievals if not properly corrected.

Aims. We present a methodology for reducing stellar contamination and instrument-specific noise from exoplanet transmission spectra using denoising autoencoders. Our goals are to enable fast, accurate corrections that improve the reliability of atmospheric parameter retrievals and to promote the use of unsupervised algorithms for efficient data processing.

Methods. We designed and trained denoising autoencoder architectures using large synthetic datasets of terrestrial (TRAPPIST-1e analogues) and sub-Neptune (K2-18b analogues) planets. We evaluated reconstruction quality using the χ^2 statistic over a wide range of signal-to-noise ratios. Furthermore, we performed atmospheric retrieval experiments on contaminated spectra to compare our deep-learning approach against standard correction methods in terms of accuracy and computational cost.

Results. Our autoencoders successfully reconstruct uncontaminated spectra, preserving essential molecular features even in low-S/N regimes. In retrieval tests, the denoising autoencoder pre-processing reduces bias in retrieved abundance parameters compared to uncorrected baselines. Notably, our method matches the accuracy of simultaneous stellar-contamination fitting while reducing computational time by a factor of three to six.

Conclusions. These results demonstrate that denoising autoencoders outperform conventional correction methods in computational efficiency while maintaining high accuracy, paving the way for their integration into future atmospheric characterization pipelines for both rocky and gaseous exoplanets.

Key words. methods: data analysis – methods: statistical – planets and satellites: atmospheres – stars: activity – techniques: spectroscopic – software: machine learning

1. Introduction

The characterization of exoplanetary atmospheres began nearly two decades ago with the pioneering detection of sodium in the atmosphere of the hot Jupiter *HD 209458 b* through transit spectroscopy using the Hubble Space Telescope (Charbonneau et al. 2002). Since then, successive observations with Hubble, Spitzer, and ground-based telescopes have revealed signatures of various compounds in the atmospheres of gas giant exoplanets, such as water vapor (Tinetti et al. 2007), methane (Swain et al. 2008), and carbon monoxide (Snellen et al. 2010). The latest array of telescopes, exemplified by the JWST, has greatly improved our observational capabilities. With an infrared range, high resolution, and increased sensitivity, it enables exact observations. The JWST has been able to detect CO₂, H₂O, Na, and CO concurrently within even individual transit spectra (Rustamkulov et al. 2023), and has allowed exploration of thermal structures in ultra-hot exoplanets via emission spectra that reveal temperature inversions and detailed molecular abundances (Coulombe et al. 2023).

Beyond gas giants, JWST has also begun probing the atmospheres of rocky exoplanets orbiting low-mass stars. The most promising candidates for transmission spectroscopy are solid exoplanets where H₂-rich atmospheres have been proposed. Re-

cently, tentative evidence for compounds such as dimethyl sulfide, a potential biosignature (Madhusudhan et al. 2023, 2025), has been found. Transmission spectra showing signatures of CH₄, CO₂, and H₂O have also been reported for planets ranging from Earth-sized to sub-Neptune-sized (Benneke et al. 2024), and a recent study of *LHS 1140 b* using JWST/NIRISS points toward an atmosphere dominated by N₂, with evidence of Rayleigh scattering and the exclusion of a H₂-rich atmosphere (Cadeux et al. 2024).

However, analysing contaminated and noisy transmission spectra presents substantial challenges. Inherent limitations in current models, including instrumental noise, uncorrected systematics, and uncertainties in molecular opacity grids, have introduced a “precision wall” that constrains the reliability of atmospheric inference (Niraula et al. 2022, 2023). In this context, one of the most significant obstacles in analysing planetary transmission spectra, especially around relatively active stars, is stellar contamination, also known as the transit light source effect (TLS).

In general, the TLS encompasses distortions introduced by photospheric heterogeneities, such as cool spots and hot faculae, which are not readily revealed by stellar photometry and must be modelled on a case-by-case basis (Rackham et al. 2018, 2019, 2023).

* Corresponding author: dsantiago.duque@udea.edu.co

This effect is notably important for rocky exoplanets orbiting M dwarfs, known for their strong magnetic activity (see e.g. Iyer & Line 2020). This was corroborated in JWST/NIRISS observations of *TRAPPIST-1 b* transits (Lim et al. 2023). Additionally, unocculted faculae have been identified, using FORS2/VLT, on WASP-69 during the transit of one of its planets, *WASP-69 b* (Petit Dit De La Roche et al. 2024).

To address TLS, various strategies have been proposed. In multiple-planet systems, a model-independent strategy using consecutive transits of sibling planets has led to an up to 2.5-fold decrease in contamination of the *TRAPPIST-1 c* transmission spectrum (Rathcke et al. 2025). The most common approach is to model TLS explicitly in atmospheric retrieval models. Lastly, several authors have employed out-of-transit stellar spectra to manage heterogeneities (Rackham & De Wit 2024; Cadieux et al. 2024).

Despite these efforts, several key challenges remain. First, current stellar spectra models frequently struggle to accurately represent low-mass stars' spectra (see e.g. Rackham & De Wit 2024). Secondly, the reduction of stellar contamination in retrieval procedures is too model-dependent. Lastly, a significant overlap between stellar and planetary parameters complicates signal separation (see e.g. Iyer & Line 2020). Therefore, with traditional methodologies, improved stellar modeling and further observations are essential for a thorough understanding of these heterogeneities and their effects on transmission spectra.

In this work, we address the aforementioned challenges by proposing a novel neural-network-based methodology. For this purpose, we designed several “autoencoders”, namely, specialized neural networks that capture the essential structure of the original transmission spectra; we trained the networks on synthetic signals and tested the resulting algorithms on simulated and realistic spectra. With this methodology, we aim, first, to enable fast and accurate corrections that improve the reliability of atmospheric parameter retrievals. Second, to promote the use of unsupervised algorithms to efficiently reduce stellar contamination and noise before retrieval procedures.

In recent years, autoencoders have found multiple applications within the astronomical community, demonstrating their effectiveness across diverse observational contexts and data types. For instance, convolutional denoising autoencoders have been successfully applied to reduce noise in individual astronomical images, effectively preserving morphological details of galaxies observed by Pan-STARRS (Bartlett et al. 2023). Similarly, Scourfield et al. (2023) employed variational autoencoders (VAEs) to enhance optical galaxy spectra from the Sloan Digital Sky Survey (SDSS), significantly improving the detection and measurement of emission-line fluxes without requiring spectral stacking.

Within the field of stellar spectroscopy, Sedaghat et al. (2023) and Kjærsgaard et al. (2023) proposed an autoencoder-based approach designed to autonomously identify and eliminate telluric contamination present in stellar spectra. This methodology effectively distinguishes atmospheric absorption characteristics from stellar signatures, achieving this separation without dependence on synthetic atmospheric models or specific details of the observational conditions.

In the domain of exoplanetary atmospheric characterization, our team has previously employed denoising autoencoders (DAE) as a core component of an ensemble learning framework designed to infer the presence of bioindicators in low-S/N spectra (Duque-Castaño et al. 2025). While those DAEs exhibited a commendable capability to reconstruct salient spectral features, that investigation was not primarily oriented towards comprehensive

denoising or high-fidelity removal of stellar contamination. For rigorous and detailed analyses of exoplanetary spectra, a more versatile, informative, and scalable DAE design is required. This is precisely the goal of this paper.

This work is organized as follows. In section 2 we summarize the transit light source formalism and derive the wavelength-dependent contamination factor ϵ_λ , which we use to generate controlled contaminated spectra. In section 3 we introduce denoising autoencoders and outline the relevant noise sources affecting transmission spectroscopy, placing our approach in the broader context of astronomical applications of AEs. In sections 4 and 5 we present our first numerical experiment: the design, training, and evaluation of a general stellar-contamination DAE (G-DAE) tailored to terrestrial-planet, including tests with realistic JWST/NIRSpec PRISM uncertainties and controlled retrieval comparisons with POSEIDON. In section 6, we extend the methodology to sub-Neptune transmission spectra and assess performance across contamination and noise regimes. We discuss limitations, domain generalization, and practical considerations for real observations in section 7. Finally, we summarize the main findings and outline future directions in section 8.

2. Stellar contamination

Stellar contamination, or more precisely, the transit light source effect¹, represents one of the most significant challenges when analysing observed transmission spectra. As was succinctly outlined in section 1, the presence of spots (cold regions) and faculae (hot regions) on the stellar surface distorts the transmission spectrum, potentially mimicking genuine planetary atmospheric signatures. In Figure 1, we schematically represent how stellar contamination alters transmission planetary spectra and illustrate the effect that the stellar spectra model has on the resulting alterations.

The wavelength-dependent effect of stellar heterogeneities in the transmission spectra can be modelled with a relatively simple formalism originally introduced by Rackham et al. (2017, 2018). It was improved to account for the general possibility that the planet also transits areas covered by those heterogeneities in Zhang et al. (2018). For completeness, we derive their formulae here and analyse the impact of this effect on transmission spectra.

By definition, the transit depth is defined as

$$D_{\text{obs}}(\lambda) \equiv \left(\frac{R_p}{R_\star} \right)_{\text{obs}}^2 = \frac{\Delta F_{\text{chord}}(\lambda)}{F_{\text{out}}(\lambda)}, \quad (1)$$

where ΔF_{chord} is the flux blocked by the planet along the transit chord and F_{out} is the integrated flux of the entire photosphere.

We assume that the host star has an area fraction f_{spot} covered by cold/dark stellar spots. For simplicity, we can also assume that the radiation coming from the spot has a blackbody spectrum with temperature $T_{\text{spot}} < T_{\text{phot}}$, where T_{phot} is the quiet photospheric temperature. On the other hand we can also have a fraction f_{fac} of the surface covered by bright/hot faculae with a blackbody temperature $T_{\text{fac}} > T_{\text{phot}}$. Taking into account the heterogeneities, the integrated flux of the star will be

$$F_{\text{out}}(\lambda) = (1 - f_{\text{spot}} - f_{\text{fac}})F_{\text{phot}}(\lambda, T_{\text{phot}}) + f_{\text{spot}}F_{\text{spot}}(\lambda, T_{\text{spot}}) + f_{\text{fac}}F_{\text{fac}}(\lambda, T_{\text{fac}}). \quad (2)$$

¹ Hereafter, and for the sake of clarity, we will use the acronym TLS and stellar contamination interchangeably for referring to the same effect.

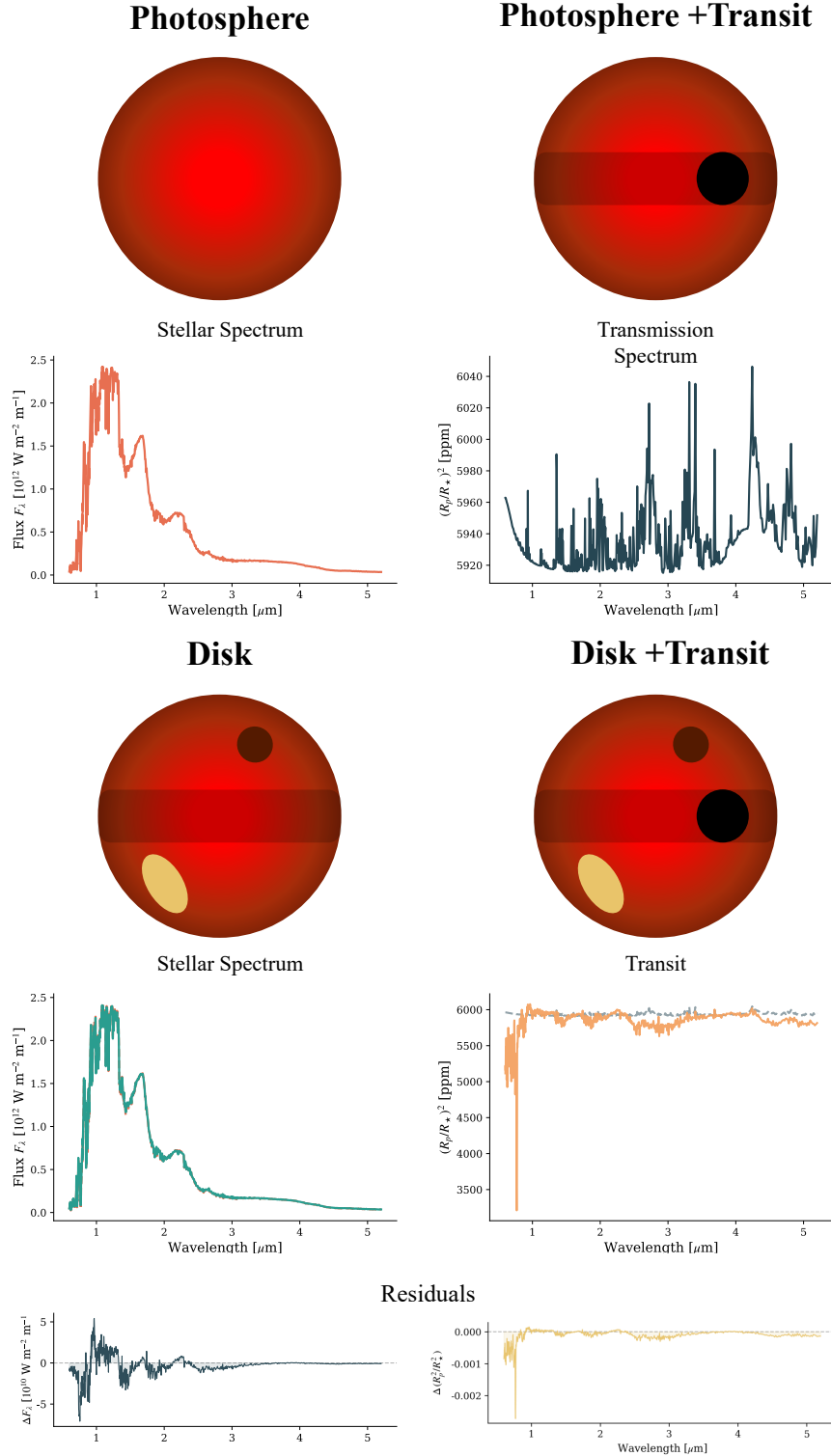


Fig. 1: Schematic representation of the effect of stellar contamination (TLS) with actual examples of the effect of TLS in simulated signals. In the left column, we show the stellar spectrum, both when the photosphere is clean (no heterogeneities, stellar spots, or faculae) and when the star exhibits heterogeneities (second and third rows). The rows show the difference (residual) between the clean and contaminated stellar spectra. The residuals have been amplified relative to the spectra to highlight regions where the effects are more pronounced. In the right column, we show the corresponding transmission spectra: in the upper half, the clean photosphere case, and in the bottom rows, the contaminated case. In all cases, we have illustrated the simpler case when the chord does not include any heterogeneity, $c_{\text{spot}} = c_{\text{fac}} = 0$ (see text).

On the other hand, and similarly, the mean specific flux behind the chord is

$$F_{\text{chord}}(\lambda) = (1 - c_{\text{spot}} - c_{\text{fac}})F_{\text{phot}}(\lambda, T_{\text{phot}}) + c_{\text{spot}}F_{\text{spot}}(\lambda, T_{\text{spot}}) + c_{\text{fac}}F_{\text{fac}}(\lambda, T_{\text{fac}}), \quad (3)$$

where c_{spot} and c_{fac} are the fraction of the surface covered by heterogeneities across the transit chord.

The change in flux produced by a planet with a projected radius $R_p(\lambda)$ will be:

$$\Delta F_{\text{chord}}(\lambda) = \left(\frac{R_p(\lambda)}{R_\star}\right)^2 F_{\text{chord}}(\lambda). \quad (4)$$

Plugging Equations 4, 3 and 2 into Equation 1 we get

$$\left(\frac{R_p}{R_\star}\right)_{\text{obs}}^2 = \left(\frac{R_p(\lambda)}{R_\star}\right)^2 \epsilon_\lambda(C), \quad (5)$$

where $C = \{f_{\text{spot}}, c_{\text{spot}}, T_{\text{spot}}, f_{\text{fac}}, c_{\text{fac}}, T_{\text{fac}}\}$ is the complete set of free parameters that characterize the TLS, and the function ϵ_λ is given by

$$\epsilon_\lambda(C) = \frac{(1 - c_{\text{spot}} - c_{\text{fac}})F_{\text{phot}}(\lambda) + c_{\text{spot}}F_{\text{spot}}(\lambda) + c_{\text{fac}}F_{\text{fac}}(\lambda)}{(1 - f_{\text{spot}} - f_{\text{fac}})F_{\text{phot}}(\lambda) + f_{\text{spot}}F_{\text{spot}}(\lambda) + f_{\text{fac}}F_{\text{fac}}(\lambda)}. \quad (6)$$

In practice, we measured $(R_p/R_\star)_{\text{obs}}^2$ but are interested in calculating $(R_p(\lambda)/R_\star)^2$. As it is evident in Equation 6, the potentially complex and less informative dependence on wavelength of ϵ_λ may obscure the very informative spectral features in $R_p(\lambda)$. It is this wavelength-dependent contamination that we aim to remove to perform a retrieval of the clean spectrum.

To mitigate the TLS, various strategies are being developed, including model-independent approaches that leverage sibling planet transits, reducing contamination for TRAPPIST-1 c by a factor of 2.5 (Rathcke et al. 2025), explicit TLS inclusion in atmospheric retrieval models, and using out-of-transit stellar spectra to characterize heterogeneities (Rackham & De Wit 2024; Cadieux et al. 2024). Despite these advances, significant limitations persist, including the difficulty that stellar models have in accurately reproducing M-dwarf spectra and the substantial degeneracy between stellar and planetary parameters (Iyer & Line 2020). Thus, improving stellar models and acquiring additional observations are essential for a precise characterization of the TLS in what we can call traditional methodologies.

3. Autoencoders for denoising transmission spectra

3.1. Noise sources

Exoplanet transit spectra are affected by multiple noise sources, including instrumental components (such as readout noise, the $1/f$ noise inherent to detectors like JWST's NIRSpec, saturation effects, and cosmic rays), astrophysical factors (such as variability and stellar spots), and other systematic errors (Jakobsen et al. 2022). In the JWST era, while the instruments offer unprecedented stability and sensitivity, a meticulous treatment of noise remains essential, particularly to correct effects such as saturation or correlated noise that can persist (Sarkar et al. 2024; Rustamkulov et al. 2023).

To address these challenges, various data reduction pipelines have been developed, such as JEXOPIPE (Sarkar et al. 2024) and other analysis frameworks. These, combined with advanced calibration techniques, have enabled many JWST observations to reach the fundamental photon-noise limit, although some residual instrumental noise can sometimes remain (Sarkar et al. 2024; Rustamkulov et al. 2023).

Nevertheless, even with optimal data reduction, the challenge of astrophysical noise persists, intrinsic to the observations and to the limitations of atmospheric models. A crucial component of this is stellar contamination. As explained in section 1, if not properly modelled and corrected, stellar contamination can introduce significant biases into the observed transmission spectrum, strongly affecting the characterization of exoplanet atmospheres and leading to erroneous interpretations of their composition and structure.

Controlling all these noise sources is crucial, as it directly impacts the accuracy and reliability of atmospheric parameter retrieval. A well-calibrated spectrum with high S/N that accounts for and mitigates astrophysical effects, such as stellar contamination, enables the detection and quantification of weak chemical components. Conversely, a spectrum dominated by noise or with poorly corrected systematics can lead to ambiguous or incorrect identification.

3.2. Autoencoders in astronomy

In general, besides the input and output layers, an autoencoder consists of two core components (see Figure 2 for a schematic representation): an encoder network, $f_\theta(X)$, characterized by a set of parameters θ , that reduces input spectrum X to a compact latent representation, Z ; and a decoder network $g_{\theta'}(Z)$ that produces an output spectrum X' . During training, the input and output spectra can be compared using various criteria. In denoising, the comparison is made between the output spectrum and the signal before noise and contamination (gray curve below the input spectrum in Figure 2).

From a theoretical standpoint, autoencoders (AEs) aim to approximate the identity function: given an input spectrum, the network should produce an output signal that is nearly identical to the input. This is achieved by incorporating constraints like bottleneck layers (e.g., reduction in the dimension of the input signal) or regularization terms (e.g., additional terms in the loss function, the function we want to minimize during training, to constrain properties of the latent space) to prevent trivial or overly simplistic solutions (see e.g. Berahmand et al. 2024).

From a spectral analysis perspective, the encoder transforms a spectrum, potentially containing hundreds of channels (even hundreds of thousands of channels in some applications), into a reduced set of latent features that capture the essential information of the original spectrum (Scourfield et al. 2023; Melchior et al. 2023). This latent representation often encapsulates the intrinsic dimensionality, i.e., the signal degrees of freedom (e.g. composition, mixing ratios, etc.) and underlying physical properties of the source (see e.g. Kjærsgaard et al. 2023). Subsequently, the decoder reconstructs the signal from this compressed representation. Training an autoencoder involves minimizing a reconstruction loss function (such as mean squared error, MSE), thereby simultaneously optimizing the parameters θ and θ' (e.g. weights and biases of neurons) of both the encoder and decoder.

Within the broader family of AE networks, denoising autoencoders (DAEs) are specifically designed to handle noisy or corrupted inputs. During training, these networks are intentionally

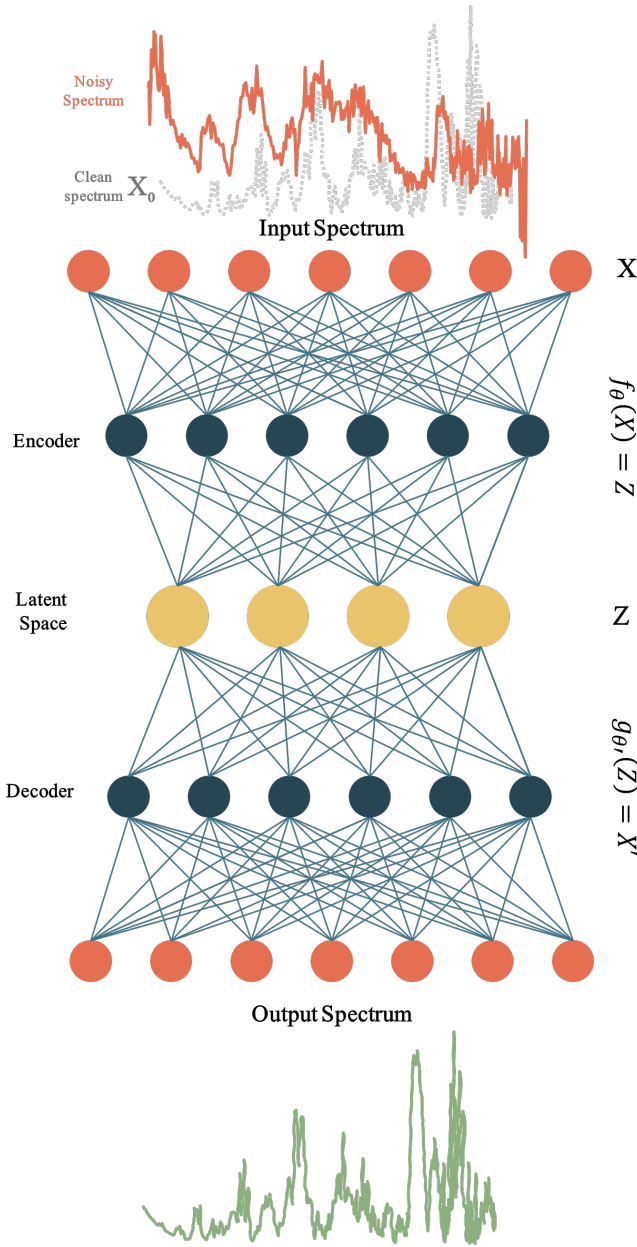


Fig. 2: Architecture of a standard Denoising Autoencoder (DAE). The input signal X is the observed transit spectrum (continuous line), which has been transformed from the original clean spectrum X_0 (dashed line) by the effect of stellar contamination. The spectrum is fed into the neural network through an encoder, composed of multiple dense hidden layers. These layers progressively compress the spectral information, ultimately producing a compact, abstract representation Z in the so-called “Latent Space”. Subsequently, the network’s decoder uses this latent representation to reconstruct a clean spectrum X' . During training, the autoencoder learns to effectively isolate and remove stellar contamination signals during encoding.

exposed to corrupted data and are asked to reconstruct the original, clean version². The theoretical rationale behind DAEs is that forcing the network to recover clean data from noisy ver-

² It is important to stress that DAEs only work if we have clean signals to train the AE. For transmission spectra, this implies that DAEs are best suited only when we work with synthetic signals.

sions helps it learn robust, invariant features rather than superficial or irrelevant variations present in raw data. This method effectively isolates and removes noise, preserving and often highlighting essential features (Morvan et al. 2022; Berahmand et al. 2024).

A key characteristic of DAEs is their implicit ability to learn the conditional distribution of clean data given noisy observations, making them particularly valuable in astronomy, where observational data frequently suffer from various sources of instrumental, atmospheric, or photon noise (Gheller & Vazza 2021).

In order to illustrate the power of DAEs, in Figure 3 we reproduce a modified version of Figure 2 in Duque-Castaño et al. (2025) that shows the result of denoising different synthetic transmission spectra of Earth-like exoplanets. This particular DAE was trained using millions of different synthetic transmission spectra of Earth-like exoplanets having free chemistry bioindicators, a single PHOENIX stellar spectra for a star with the properties of TRAPPIST-1, and the model of stellar contamination described in section 2. Additionally, the input spectra were contaminated with Gaussian noise, with S/N ranging from 1 to 10.

The result is notable. Beyond the underlying simplifications in the numerical experiment, the capability of a general DAE to reconstruct a clean spectrum without explicitly modeling contamination and noise motivates us to explore the power of DAEs in more general and realistic settings, such as those we study in this work.

Nevertheless, the flexibility and unsupervised nature of autoencoders, combined with recent advances in neural architectures—such as the integration of attention mechanisms or convolutional layers (Morvan et al. 2022; Sedaghat et al. 2023) position them as powerful tools for addressing the increasing complexity and scale of astronomical datasets. Their capability to extract compact, physically meaningful representations from noisy observations shows great promise for upcoming large-scale surveys and next-generation astronomical instrumentation.

4. A general stellar contamination DAE (G-DAE)

For our first numerical experiment, we explore the case of Earth-like exoplanets orbiting M-dwarfs and containing potential biosignatures and/or bioindicators as we did in Duque-Castaño et al. (2025). For this purpose, we model the case of *TRAPPIST-1 e* for which we assume a diverse set of atmospheric compositions having at least four molecular species, CO₂-N₂ (fill gases), CH₄, O₃, and H₂O, that produce the strongest spectral signatures (see e.g. Kaltenegger & Traub 2009; Lustig-Yaeger et al. 2023).

For the sake of completeness, we reproduce in Figure 4 a theoretical spectrum of a *TRAPPIST-1 e* analogue, similar to the spectrum in Figure 3 of Duque-Castaño et al. (2025). To compute this spectrum, we assume that the planet’s mixing ratios are similar to those of Earth’s surface during the Proterozoic.

We call this general-purpose DAE for removing stellar contamination a G-DAE (pronounced “yee-dai”).

4.1. Model architecture

The first G-DAE was developed in KERAS (Chollet 2015) with a TENSORFLOW backend (Abadi et al. 2015). It receives as input a normalized vector of intensities at 385 wavelength points. The network processes the data through a symmetric en-

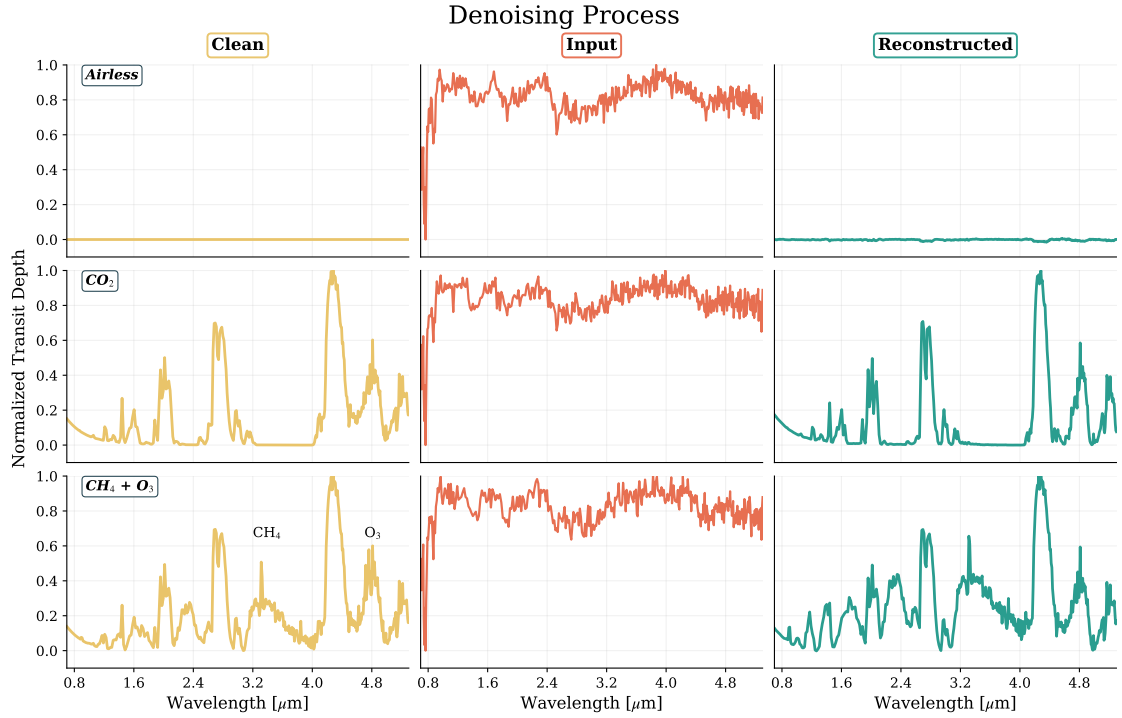


Fig. 3: Examples of the autoencoder implementation designed to mitigate stellar contamination in three representative synthetic transmission spectra: an airless planet (first row), a planet with a CO₂-rich atmosphere (second row), and a planet with potential biosignatures (third row). The input spectra have an S/N of 3 and include stellar contamination levels of $f_{\text{spot}} = 0.08$ and $f_{\text{fac}} = 0.54$. The panels in the first column display the synthetic spectra free from noise and contamination; the second column shows the input spectra affected by noise and contamination; and the third column presents the reconstructed spectra returned by the autoencoder.

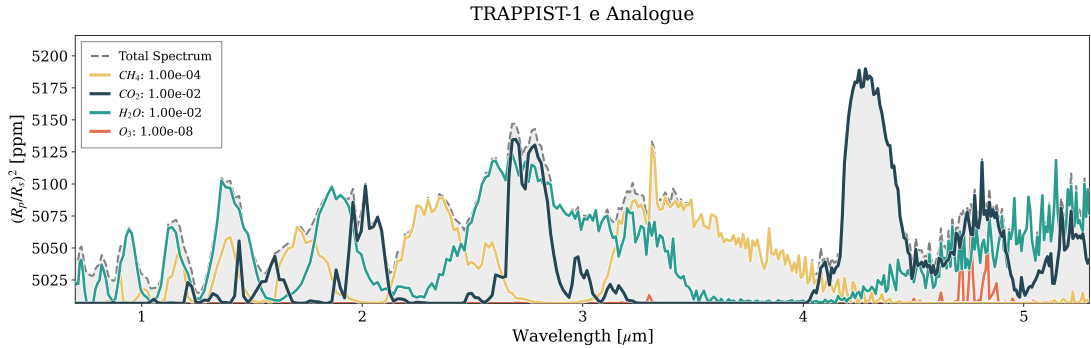


Fig. 4: Clean transmission spectrum of a *TRAPPIST-1 e* analogue with an arbitrary (non-equilibrium) composition. The contribution of each gas has been plotted as a continuous, thick line, while the signal of the fill gases (CO₂ and N₂) is shown as a thinner line in the background. The combined spectrum is limited by the dashed line, and the shaded region is also shown in the background.

coder-decoder: the encoder comprises three fully connected layers of 512 units, followed by two layers of 300 units; the decoder mirrors this architecture and ends with a linear layer that projects back to 385 outputs. All hidden units use the Swish activation $f(x) = x/(1 + e^{-x})$ (see e.g. Géron 2023). To mitigate overfitting, we apply dropout with a rate of 0.5 after every hidden layer and L2 (weight-decay) regularization with a coefficient $\lambda = 10^{-6}$ on all dense kernels except the final output layer.

The specific set of hyperparameters for our G-DAE resulted from a grid search varying depth/width, dropout rate, and the L2 coefficient, training on the full spectra set (see below) and selecting the configuration that minimized the ‘‘Mean Absolute Error’’ (MAE). As noted in section 3, the MAE is computed between the reconstructed spectrum and its corresponding clean target

prior to adding stellar contamination and noise; the L2 penalty is added through the layer regularizers while MAE remains the primary reconstruction loss.

4.2. Model training

To generate the training set, we use the same methodology as described in Duque-Castaño et al. (2025). For completeness, we briefly outline the generation methodology below.

Planetary atmosphere chemistries contain none, one, two, or all of the three key molecules, CH₄, O₃, and H₂O. Mixing ratios for each species were drawn from eight discrete values distributed log-uniformly between 10⁻⁸ and 10⁻¹. These were combined with three representative isothermal atmospheric temper-

Table 1: Distribution of training spectra for the general stellar-contamination DAE. Each row corresponds to a different S/N used in the training set, with 0 denoting noise-free spectra. Columns are labeled with three-digit binary codes indicating the presence (1) or absence (0) of CH_4 , O_3 , and H_2O , respectively (e.g., “010” indicates no CH_4 , presence of O_3 , and no H_2O). The “Airless” column corresponds to flat spectra with no atmospheric absorption. Values in each cell are in thousands and represent the total number of spectra (including noisy realizations and all stellar contamination scenarios) generated for each atmospheric configuration.

S/N	000	100	010	001	110	101	011	111	Airless
1	60	48	48	48	38.40	38.40	38.40	61.44	20
3	60	48	48	48	38.40	38.40	38.40	61.44	20
6	45	36	36	36	28.80	28.80	28.80	46.08	15
10	30	24	24	24	19.20	19.20	19.20	30.72	10
0	90	72	72	72	57.60	57.60	57.60	76.80	40

atures of 200 K, 287 K, and 400 K. The baseline fill gas atmosphere consisted of N_2 with a CO_2 mixing ratio of 10^{-3} , representing an intermediate case between modern Earth and early Earth conditions. Finally, we also included an airless planet that produces flat spectra with no atmospheric absorption. All atmospheres were assumed to have an Earth-like surface pressure of 1 bar. For the vertical structure, we use a 100-layer model.

For each base spectrum (fixed chemistry, surface pressure, and temperature profile), multiple noisy realizations were produced at five S/N values: 0 (noise-free), 1, 3, 6, and 10. Stellar contamination was simulated by multiplying each spectrum by precomputed wavelength-dependent ϵ_λ (see Equation 6). For this purpose, we used the POSEIDON code (MacDonald & Madhusudhan 2017; MacDonald 2023). In all cases, we assume for simplicity that no heterogeneities were found in the chord, i.e., $c_{\text{spot}} = c_{\text{fac}} = 0$. For the coverage fractions we combined three values of $f_{\text{spot}} = 0.01, 0.08$, and 0.26 , and three values $f_{\text{fac}} = 0.08, 0.54$, and 0.70 , following the suggestions by Rackham et al. (2018).

Nine contaminated scenarios and one uncontaminated case were used, producing ten versions of each spectrum. For example, a family of spectra with one molecular species at S/N = 1 starts from 8 possible mixing ratios for that molecule, combined with 3 different temperatures, giving $8 \times 3 = 24$ base spectra. The same configuration is then replicated across 10 stellar-contamination cases (nine contaminated plus one uncontaminated) and 200 noisy realizations, yielding $((8 \times 3) \times 10) \times 200 = 48,000$ spectra.

The Table 1 summarizes the dataset composition across S/N levels and atmospheric configurations. Values are expressed in thousands and account for all noisy realizations and stellar contamination scenarios. The complete training set comprised 1,897,680 spectra.

To fit the model, the data were split into 80% for training and 20% for validation. Learning was carried out using the Adam optimizer (see e.g. Géron 2023) with a learning rate of 10^{-5} , a batch size of 64, MAE loss, early stopping with a patience of 5 epochs, and a maximum of 100 epochs. Most of these optimization parameters were determined by systematic experimentation.

Once the training set of synthetic spectra was generated and the algorithms were trained to denoise them, we proceeded to test the neural networks on different test sets. This process involves generally two steps: the first step is “model validation”, in which the algorithms are subject to a limited set of spectra

intended to assess their general performance and modify, if required, the parameters of the algorithms to obtain the desired result; the second step is “model evaluation” in which the algorithms are subject to a more robust set of tests and confirm whether they achieve the task for which they were designed..

4.3. Model validation

During the training, the network reached a validation MSE of 0.00433^c and a test coefficient of determination $R^2 = 0.854$. These results demonstrate that the model preserved the main molecular absorption features while effectively reducing noise and contamination.

We confirm the effectiveness of the reconstruction and the previous conclusion with a visual inspection of some of the reconstructed signals (see Figure 3).

4.3.1. Quantifying uncertainties

To quantify uncertainty in the reconstructed exoplanet transmission spectra from our G-DAE, we adopt a Bayesian deep learning framework. This approach aims to systematically characterize and separate the sources of uncertainty, distinguishing between two primary types: aleatoric and epistemic. Aleatoric uncertainty refers to noise inherent in the observations. It represents variability from instrumental or environmental sources (Kendall & Gal 2017). This form of uncertainty cannot be reduced, even with more extensive data used during model training or additional observational examples, because it reflects fundamental limitations of the measurement process, including sensor inaccuracies and stochastic perturbations in the signal. In contrast, epistemic uncertainty accounts for ignorance in the model parameters, arising from limited training data or model approximations, and can be mitigated as more data become available (Kendall & Gal 2017; Gal & Ghahramani 2016). Estimating both uncertainties is crucial in astronomical applications such as exoplanet spectroscopy, where overly confident predictions can lead to erroneous interpretations of atmospheric compositions or planetary properties. As highlighted by Kendall & Gal (2017), failing to model these uncertainties can lead to disastrous consequences, analogous to misclassifications in computer vision tasks, underscoring the need for robust uncertainty quantification to enhance model reliability and inform downstream analyses.

To estimate epistemic uncertainty without retraining the G-DAE, we employ Monte Carlo Dropout, which treats dropout layers in the neural network as a variational approximation to Bayesian inference in deep Gaussian processes (Gal & Ghahramani 2016). By performing multiple forward passes with dropout activated during inference (e.g., 100 iterations), we sample from the approximate posterior distribution over the model weights. The predictive mean is computed as the average of these reconstructions, while the variance across samples quantifies the epistemic uncertainty, capturing model ignorance in regions with sparse training data or in extrapolation (Gal & Ghahramani 2016). This approach ensures computational efficiency while preserving fidelity to the trained model, as dropout marginalizes over the model’s parameters without additional optimization, thereby providing a practical Bayesian approximation that improves predictive log-likelihood and root-mean-square error compared to deterministic models.

^c Although our loss function during the learning process was the MAE, we use MSE as the validation metric.

Aleatoric uncertainty is derived directly from the instrumental noise profiles of the input spectra. However, simply adopting the full magnitude of these observational error bars would yield overly conservative estimates that fail to reflect the G-DAE’s effective denoising capabilities. Conversely, ignoring this noise component entirely would lead to excessive optimism and unrealistically narrow error bars. Consequently, we define the aleatoric uncertainty as the instrumental noise scaled by a factor of 0.5. This scaling was found to strike a necessary balance: it prevents overestimating errors inherent in raw data while maintaining sufficient width to avoid underestimating the residual variance, ensuring that the uncertainty bounds remain statistically robust. Finally, by summing the variances of the aleatoric and epistemic components, we obtain the total predictive uncertainty (Kendall & Gal 2017).

5. Model evaluation

To evaluate the performance of our DAE, we conducted several numerical experiments using test spectra different from those used in the validation process (see subsection 4.3). We called this new set of spectra, “evaluation set”.

To compare the reconstructed and the clean original spectrum, we used the chi-square statistic (χ^2) defined by the equation

$$\chi^2 = \sum_i \frac{[S(\lambda_i) - S_r(\lambda_i)]^2}{\Delta S(\lambda_i)^2}, \quad (7)$$

where $S(\lambda_i)$ is the clean, uncontaminated spectrum in physical units (transit depth), $S_r(\lambda_i)$ is the G-DAE-reconstructed spectrum after rescaling from normalized space, and $\Delta S(\lambda_i)$ is the wavelength-dependent uncertainty returned by PANDExo.

We used the reduced chi-square (χ_r^2) as a key metric

$$\chi_r^2 = \frac{\chi^2}{N - p}, \quad (8)$$

where N is the number of spectral points and p is the number of fitted parameters. Since the AE is non-parametric, we set $p = 0$.

An ideal $\chi_r^2 \approx 1$ indicates residuals consistent with the noise model. Values of $\chi_r^2 \gg 1$ generally indicate model–data mismatch or underestimated errors. On the other hand, χ_r^2 values much lower than 1 can indicate either over-smoothing, the loss of real features, or overestimation of signal errors. Since $\Delta S(\lambda_i)$ are the uncertainties of the noisy spectra and not the uncertainties of the denoised one, values of $\chi_r^2 < 1$ are expected. However, extremely low values of the statistics may indicate that genuine spectral structure has been removed during the denoising process.

5.1. Denoising with realistic instrumental noise

For the first experiment, we evaluated our G-DAE using spectra degraded with PANDExo-generated noise. For this case, we simulated JWST/NIRSpec PRISM time-series observations covering the spectral range 0.69–5.3 μm .

The simulation employed the PHOENIX stellar SED from PANDExo using the TRAPPIST-1 parameters. We note that, for the training set, we also used the PHOENIX database, but within the context of the TAUREX tools. Since both tools may use the spectra database differently, for instance by employing different grid interpolation procedures or parameters, the spectra used for

training and testing may differ slightly, making the denoising procedure more challenging.

We simulated JWST/NIRSpec in the PRISM mode with the SUB512 subarray and $\text{NGROUP} = 6$ (STScI 2025a,b; Lustig-Yaeger et al. 2019). We set the observation baseline to three times the transit duration (including pre- and post-transit phases), matching TRAPPIST-1 e parameters. The number of transits spanned a broad range of values (2–100). For each spectrum, PANDExo returns wavelength-dependent 1σ uncertainties, which are important for computing the χ^2 statistic (see below).

Figure 5 shows representative reconstructions using G-DAE of different types of transmission spectra. In all scenarios, the application of the G-DAE reduces both contamination and noise, producing flatter residuals and much closer matches to the clean spectrum. This is reflected in very low values of χ_r^2 for the reconstructed signal, compared with the same statistics for the noisy case.

5.2. Quantitative assessment of model performance

To evaluate the model’s performance over a wider range of conditions, we apply the G-DAE to spectra with different noise levels, i.e., assuming different numbers of transits per spectrum. The larger the number of transits, the lower the noise level. For each spectrum, we apply different levels of contamination and use the G-DAE to reconstruct the original signal. For each signal we compute, as before, realistic instrumental noise. We show the results of this in Figure 6. As a side note, for producing this figure, we apply the G-DAE to a total of 3×10^6 spectra, and it took less than 5 minutes in a Core i5 with an AMD Ryzen7 5700X3D processor (8 cores/16 threads, 3.0 GHz) PC to obtain the reconstructed signals. This provides an estimate of the time efficiency of this approach.

Not only do the values of the χ_r^2 stay close to the theoretical limit of 1, which demonstrates that the reconstructed spectra are almost equal to the original ones inside the irreducible errors of the method, but the value of the statistic is very stable against the increase in the noise levels (reduction in the number of transits). In other words, for the G-DAE, the reconstruction of the signal for a couple of transits is almost as good as the reconstruction in the case of tens of them.

Counterintuitively, when the number of transits is lower, the performance of the model, as measured by the reduced chi-square, improves. This effect, however, is the result of the intrinsic sensitivity of the χ_r^2 to any deviation of the reconstructed signal with respect to the original one when the noise level is low. The results of a retrieval procedure of low-noise signals produce small errors in the resulting mixing ratios.

It is interesting to notice that despite being trained solely with constant, wavelength-independent Gaussian noise parametrised by S/N, the G-DAE performs comparably on PANDExo-degraded spectra—whose uncertainties vary with wavelength. This demonstrates robustness to noise-model mismatch and a useful degree of domain generalization.

5.3. Comparative evaluation of retrieval with POSEIDON

It is essential to evaluate whether the G-DAE provides a tangible contribution to atmospheric retrieval under conditions of stellar contamination. To this end, we designed a controlled experiment in which all pipelines faced the same synthetic observation, varying only the contamination level and the number of transits (size of the observational campaign or level of resulting instrumental

Comparison of spectra — 10 transits

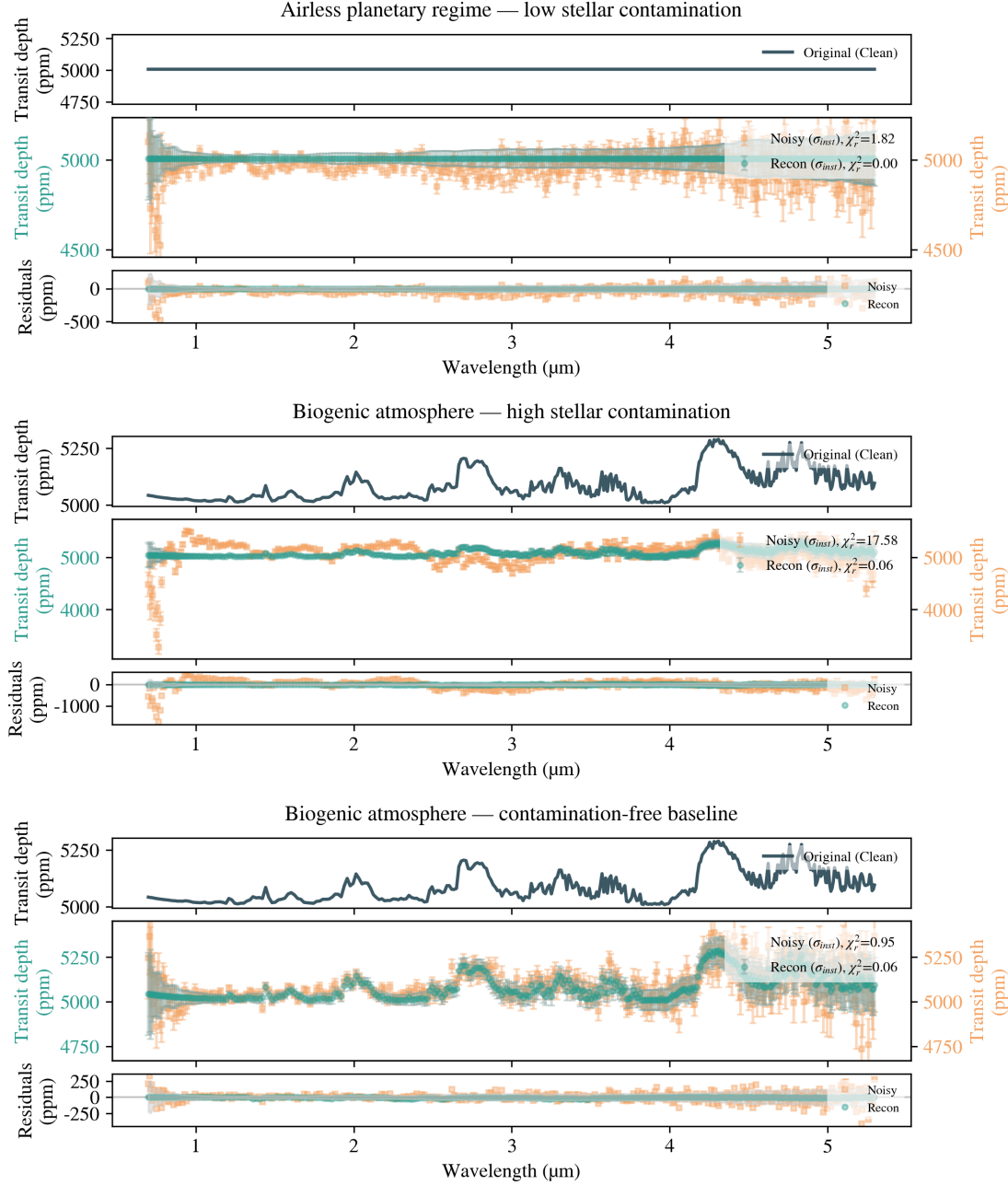


Fig. 5: Comparison between noisy and contaminated input spectra (square markers with error bars) and the reconstructions performed by our autoencoder networks (round markers) for a TRAPPIST-1e analogue with different atmospheric compositions and stellar contamination, when observed with JWST NIRSpec using ten transits. Each plot shows the original clean spectra (upper panel), the noisy and reconstructed spectra (middle panel), and the residuals for both the contaminated and reconstructed spectra (bottom panel). The y-axis scales for the transit-depth and residual plots in the noisy (right) and reconstructed (left) signals differ to highlight the disparities between the two spectra and the original spectrum. We consider three planetary scenarios: an airless planet (first row), a planet with a biogenic atmosphere but no stellar contamination (second row), and the same planet with the maximum stellar contamination.

noise). This setup allows for a direct comparison of accuracy and computational cost across three distinct strategies.

As a test case, we employed a synthetic “CO₂-only” spectrum, with N₂ as the background gas and CO₂ as the sole active absorber. The spectrum was sampled at 385 wavelength channels spanning 0.69–5.3 μm, with uncertainties generated by PANDExo

configured for JWST/NIRSpec PRISM. Two different sizes of the observational campaign were considered, 10 and 100 transits, together with four stellar surface configurations: the uncontaminated case ($f_{\text{spot}}, f_{\text{fac}}$) = (0.00, 0.00) and three pairs representing low, moderate, and high contamination: (0.01, 0.08), (0.08, 0.54), and (0.26, 0.70). Thus, the retrieval experiments en-

χ^2_r Analysis: Impact of Stellar Activity

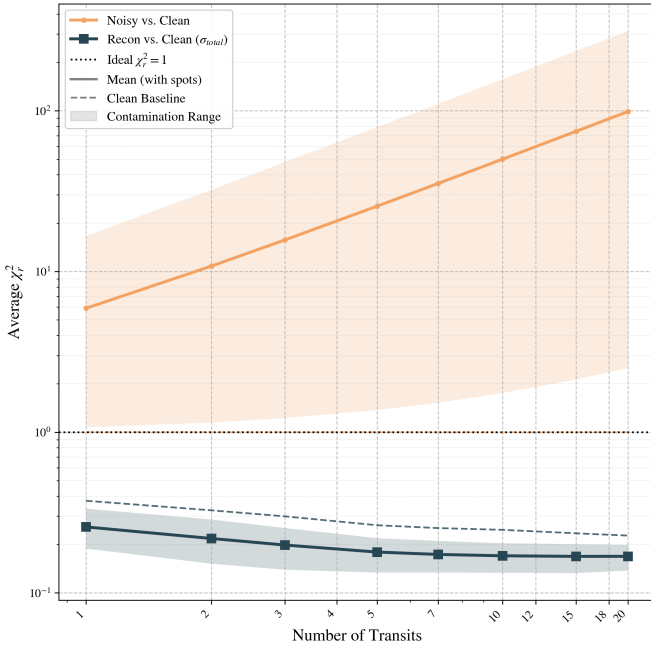


Fig. 6: Average reduced chi-square χ^2_r (continuous line) for G-DAE reconstructed spectra as a function of the number of transit (noise level). The shadowed band around the average represents the range of stellar contamination considered in our numerical experiments. To give an idea of how good the reconstruction is in the scale of the χ^2_r , we show with a dashed line the value of the statistic when comparing the uncontaminated noisy spectra with the original one.

compassed both the clean scenario and cases affected by stellar heterogeneity.

The results of the experiments are shown in Figure 7 (see below for interpretation). The three retrieval strategies compared were: (i) Chemistry-only (**Chem.**), where the forward model ignores stellar contamination; (ii) Contamination plus Chemistry (**Cont.+Chem.**), in which stellar spots and faculae are explicitly modelled and retrieved; and (iii) G-DAE and Chemistry-only retrieval (**G-DAE+Chem.**), where the contaminated spectrum is first corrected with the autoencoder and then retrieved using a forward model that also ignores contamination, as in (i).

All retrievals were conducted with POSEIDON using an isothermal, cloud-free transmission model with 100 layers ($P_{\text{ref}} = 1$ bar). The state vector included as free parameters the \log_{10} -VMRs (Volume Mixing Ratios) of H_2O , CH_4 , CO_2 , and O_3 , the isothermal temperature T , and the reference planetary radius $R_{p,\text{ref}}$ at 1 bar. The mixing ratio of N_2 was fixed by closure. In the training set, the VMR of CO_2 was set at two discrete levels: absent or present.

The atmospheric and stellar uniform priors employed are summarized in Table 2.

Wavelength-dependent contamination factors ϵ_λ (see Equation 6) were computed from PHOENIX stellar atmosphere models. Sampling was performed with MULTINEST ($N_{\text{live}} = 500$), parallelized with MPI across 12 processors. We assumed Gaussian likelihoods, with wavelength-dependent 1σ uncertainties calculated with PANDExo. Computations were carried out on a work-

Table 2: Priors used in the retrieval experiments. The range indicates that priors are uniform.

Parameter	Range
$\log_{10} \text{VMR}(\text{H}_2\text{O}, \text{CH}_4, \text{O}_3)$	[-8, -1]
$\log_{10} \text{VMR}(\text{CO}_2)$	[-5, -1]
T (K)	[200, 400]
$R_{p,\text{ref}}$	$[0.85, 1.15] \times R_{p,\text{true}}$
f_{spot}	[0, 0.26]
f_{fac}	[0, 0.70]
T_{phot}	$[0.9, 1.1] T_s$
T_{spot}	$[0.8, 0.95] T_s$
T_{fac}	$[T_s, T_s + \Delta T_{\text{fac}}]$

station equipped with an AMD Ryzen 7 5700X3D processor (8 cores/16 threads, 3.0 GHz).

For simplicity, we show in Figure 7 the results of our experiments for the case of only ten transits (reference case). We have verified that the results and conclusions derived from 100 transits (see below) do not differ significantly from the reference case.

In the top panel of Figure 7, we see that the retrieval of both the contamination parameters and chemistry (Cont.+Chem. procedure, green curves) requires the highest computation times. Those times increase with both contamination level and number of transits (not shown). In contrast, the retrieval of chemistry without fitting contamination (Chem. approach, orange curves) runs faster but yields worse fits, i.e., it has systematically larger MSE (middle panel). The chemical retrieval after applying the G-DAE (G-DAE+Chem. pipeline; red curves) consistently yields lower run times, lower MSE, and lower χ^2 values across all scenarios.

The middle panel, corresponding to the mean squared error (MSE), demonstrates that, as expected, Chem.-only loses explanatory power as stellar contamination intensifies. In the case of Contam.+Chem. The effect of contamination is mitigated to some extent, but errors still increase in heavily contaminated scenarios. In contrast, preprocessing the input spectrum with the G-DAE ensures that the MSE remains low and nearly invariant across all contamination levels.

Finally, the bottom panel presents the reduced χ^2 values. For contaminated cases at 100 transits (not shown), both Chem.-only and Contam.+Chem. attain elevated values, indicating model–data mismatches. By comparison, G-DAE+Chem. consistently yields low and stable values, consistent with the expected noise model. Taken together, these findings demonstrate that incorporating the G-DAE constitutes the most effective approach to preserving both retrieval accuracy and computational efficiency, even under high contamination and high signal-to-noise conditions.

5.4. Dependence on atmospheric chemistry

To validate our G-DAE across diverse atmospheric compositions, we performed realistic retrievals of the volume mixing ratios (VMR) of planets with diverse compositions using the retrieval strategies described in the previous section.

Figure 8 shows the posterior medians (with 1σ intervals) of the \log_{10} VMR for CO_2 , CH_4 , O_3 , and H_2O across four photospheric-heterogeneity configurations parametrised by the spot and facula coverage fractions ($f_{\text{spot}}, f_{\text{fac}}$) (including the clean case 0/0).

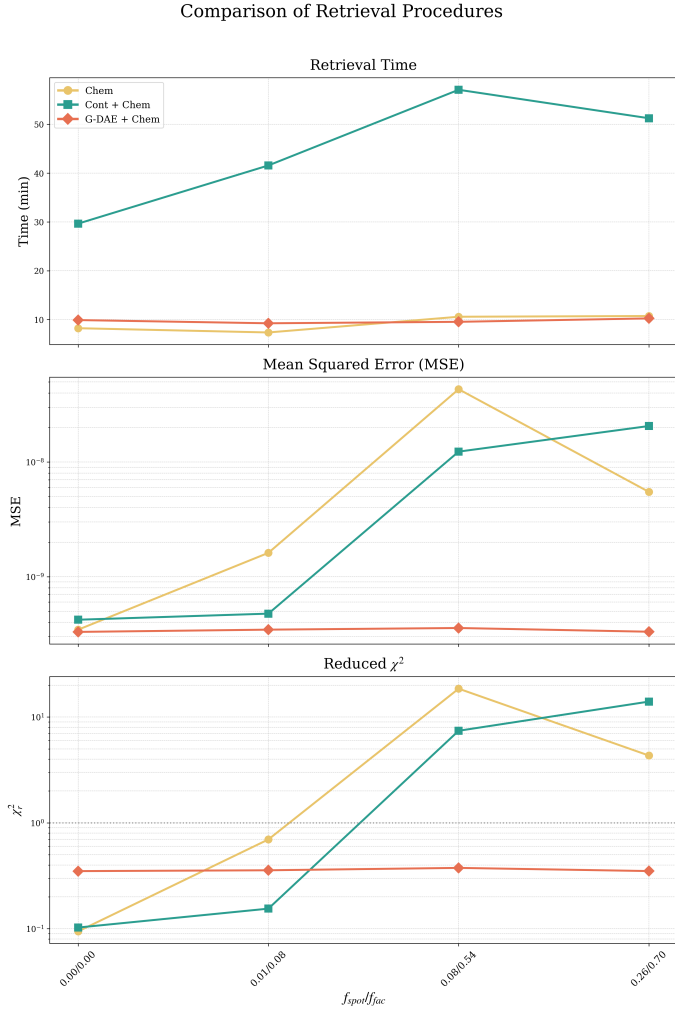


Fig. 7: Comparative evaluation of three retrieval strategies under four stellar-surface configurations: the uncontaminated case (0.00, 0.00) and three contamination levels (0.01, 0.08), (0.08, 0.54), and (0.26, 0.70). Colours denote methods (orange = Chem.; green = Cont.+Chem.; red = G-DAE+Chem.). **Top:** wall-clock time. **Middle** (log scale): mean squared error (MSE) between the retrieved model and the reference spectrum. **Bottom** (log scale): reduced χ^2 .

In this experiment, the lower bound of the prior (10^{-8}) is taken to represent the absence of the molecule (see Table 2). Because a retrieval yields a posterior distribution broadened by instrumental noise, the median may lie slightly above the -8 level in \log_{10} VMR even when there is no signal; this shift is a statistical effect of posterior broadening and should be interpreted as non-detection (an upper limit consistent with the prior).

Overall, G-DAE preprocessing + Chem.-only yields abundances more consistent and closer to the reference value for all species and contamination levels: increasing from 10 to 100 transits primarily reduces the uncertainties without appreciable shifts in the medians. By contrast, the strategies without preprocessing (no G-DAE) exhibit biases that grow with stellar heterogeneity. For CH₄, these strategies tend to overestimate the VMR by several orders of magnitude; for O₃, Stellar contamination + chemistry shows pronounced false positives in the most contaminated case, with biases that also come with narrower intervals at 100 transits. CO₂ (truth $\sim 10^{-3}$) is recovered robustly with G-DAE, whereas it drifts with contamination under the strategies with-

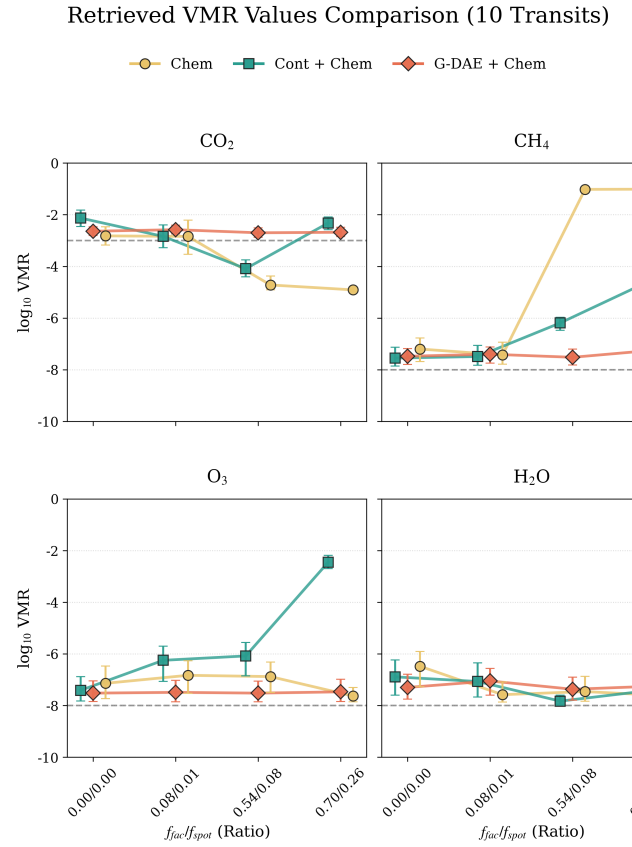


Fig. 8: Retrieved \log_{10} volume mixing ratios for CO₂, CH₄, O₃, and H₂O under four stellar-surface configurations with coverage fractions $(f_{\text{spot}}, f_{\text{fac}}) \in \{(0.00, 0.00), (0.01, 0.08), (0.08, 0.54), (0.26, 0.70)\}$. The x-axis shows $f_{\text{fac}}/f_{\text{spot}}$. Colours indicate retrieval pipelines: Chemical-only (Chem.); Stellar contamination + chemistry (Cont. + Chem.); and G-DAE preprocessing + chemical-only (G-DAE+Chem.). Points are posterior medians with 1σ intervals; The gray dashed horizontal line marks the ground-truth abundance used to generate the synthetic spectrum.

out preprocessing. Only the retrieval of H₂O remains relatively stable in all cases.

6. Other planetary cases

The case of terrestrial planets with potential biosignatures around M-dwarfs and the benefits of using neural networks, in particular autoencoders, for processing and analysing transmission spectra have been extensively demonstrated first in Duque-Castaño et al. (2025) and in previous sections. However, there are other cases in which the potential of these techniques may be more apparent in the field. In particular, the analysis of transmission spectra of sub-Neptunes and jovian planets, which, owing to their abundance and/or size, produce much more common and stronger signals, offers the most promising application of the techniques developed in this work.

In the following sections, we extend our workflow to the case of sub-Neptunes, which are a class of exoplanets with radii between 1 and 4 Earth radii, that, according to population studies (see Parc et al. 2024 and references therein), represent a prevalent type of planet in the Galaxy. These worlds offer a unique opportunity for in-depth characterization of intermediate-sized

Table 3: System parameters of *K2-18 b* (Howard et al. 2025), the model planet system for the numerical experiments of sub-Neptune cases.

Star (<i>K2-18</i>)	
Radius (R_{\odot})	0.468
Mass (M_{\odot})	0.495
T_{eff} (K)	3500
Planet (<i>K2-18 b</i>)	
Radius (R_{\oplus})	2.461
Mass (M_{\oplus})	7.2
Semi-Major Axis (au)	0.1429

exoplanets' interiors and atmospheres (Hu et al. 2025; Liu et al. 2025; Guzmán-Mesa et al. 2022; Parc et al. 2024) and could also offer interesting possibilities for the search for biosignatures (see Madhusudhan 2024 and references therein).

6.1. A model case for sub-Neptunes

As we did for the case of terrestrial planets with *TRAPPIST-1 e*, we selected a model case to analyse sub-Neptunes' transmission spectra. Due to the interesting challenges inherent in analysing its spectrum and the recent interest in the planet, we use the potential hycean planet *K2-18 b* (Madhusudhan et al. 2023) as a model case.

K2-18 b is a sub-Neptune orbiting within the habitable zone of its host star, an earlier-type red dwarf (Hu et al. 2025) (see Table 3 for a summary of the planetary and stellar properties). With a mass of 7.2 Earth masses and a radius of ~ 2.5 Earth radii, the location of *K2-18 b* within its star's habitable zone suggests the potential for liquid water and, consequently, some prospects of habitability (Tsiaras et al. 2019; Madhusudhan 2024; Madhusudhan et al. 2025). This has made *K2-18 b* a prime candidate for scrutinizing the atmospheric composition and internal structure of habitable sub-Neptunes, especially around M dwarfs (see e.g. Liu et al. 2025).

The James Webb Space Telescope has significantly advanced the characterization of *K2-18 b*'s atmosphere, revealing the presence of several chemical signatures (Madhusudhan 2024; Madhusudhan et al. 2023). Specifically, JWST observations have detected spectroscopic signatures indicating water vapour, methane, and carbon dioxide in its atmosphere (Madhusudhan 2024; Liu et al. 2025). These findings reinforce the hypothesis that *K2-18 b* could be a "hycean world" (Madhusudhan et al. 2023, 2021), namely, planets characterized by a hydrogen-rich atmosphere enveloping a water-rich interior that might even host a liquid water ocean (Hu et al. 2024; Madhusudhan et al. 2025). Such an environment, featuring an ocean-covered surface beneath a thin H_2 -rich atmosphere, positions *K2-18 b* as a significant target in the search for extraterrestrial life, especially given its potential for surface liquid water at pressures and temperatures similar to Earth's oceans (Madhusudhan 2024).

Although, as it has been extensively argued in this work and the references herein, stellar contamination from the host star can often interfere with transit spectroscopy, *K2-18 b*'s M dwarf host star offers a unique advantage due to its relatively quiet nature compared to more active late-type M-dwarfs (Madhusudhan 2024). However, accurate atmospheric retrieval for planets orbiting such stars still requires accounting for potential stellar

activity, which can introduce variability into spectroscopic data (Rackham et al. 2023).

Although *K2-18 b* is an interesting scientific target for itself, the purpose of using this planet as a model case does not imply that our conclusions are restricted to this particular planet. Our main aim is to use the well-known properties of K2-18 and one of its planets to synthesize planetary analogues for training our algorithms and to gain insights into their performance when cleaning and decontaminating sub-Neptune transmission spectra.

6.2. Atmospheric composition

To model the atmosphere of our mock sub-Neptunes, we adapted the architecture of the *ARIEL Data Challenge* (ABC) dataset described in Changeat & Yip (2023). Synthetic spectra were generated using MultiREx framework (Duque-Castaño et al. 2025) with stellar and planetary parameters taken from Howard et al. (2025).

All the mock planets have well-mixed, free-chemistry, and cloud-free (at least above a base pressure of 10 bars) atmospheres. As in the case of terrestrial planets, we assume an isothermal atmospheric profile here. In contrast to the terrestrial planet case, we used a finer grid of atmospheric temperatures, ranging from 250 K to 450 K in 50 K increments. For the top pressure, we use a fiducial value of 10^{-3} bar. The fill gases are those of primary atmospheres of H_2 and He, and hence, for modeling the transmission spectrum, we included collision-induced absorption (CIA) features for H_2 - H_2 and H_2 -He (Gordon et al. 2022).

Following the ARIEL Data Challenge specifications, we use only four molecular species: CH_4 (with a log 10 VMR in the range from -8 to -1), CO_2 (with a log 10 VMR in the range from -7 to -2), H_2O (with a log 10 VMR in the range from -10 to -1) and NH_3 (with a log 10 VMR in the range from -7 to -2). The molecular absorption cross-sections were taken from ExoMol (Chubb et al. 2021; Tennyson et al. 2016). We excluded CO because, at the noise levels of our numerical experiments, its bands mostly overlap with those of CO_2 , and their strengths are too low to justify the additional computational cost of generating additional synthetic spectra.

In Figure 9, we show the synthetic clean spectrum of a mock sub-Neptune having an atmospheric composition in the ranges used for training our algorithms. The specific mixing ratios were chosen to highlight the most salient spectral signatures of the chemical species and do not necessarily reflect the equilibrium abundances of the molecules. We can distinguish in the mock spectrum a wide CH_4 band around $3.5\ \mu m$, which dominates the spectrum in that region. Also noticeable are the bands of CO_2 around 2, 2.8, 4.3, and $4.8\ \mu m$. At least one band of NH_3 may be salient in the region of $3\ \mu m$, while water spectral signatures dominate the high-end of the spectrum.

As we did in the terrestrial planet model case, we also included in the sample of mock sub-Neptunes, on the one hand, planets having some or most of the gases completely absent. And, on the other hand, planets with flat transmission spectra. Conceptually, the latter planets would correspond to sub-Neptunes with very high, opaque clouds; numerically, those flat spectra are simply signals of equal strength (the nominal radius of the planet) at all sampled wavelengths.

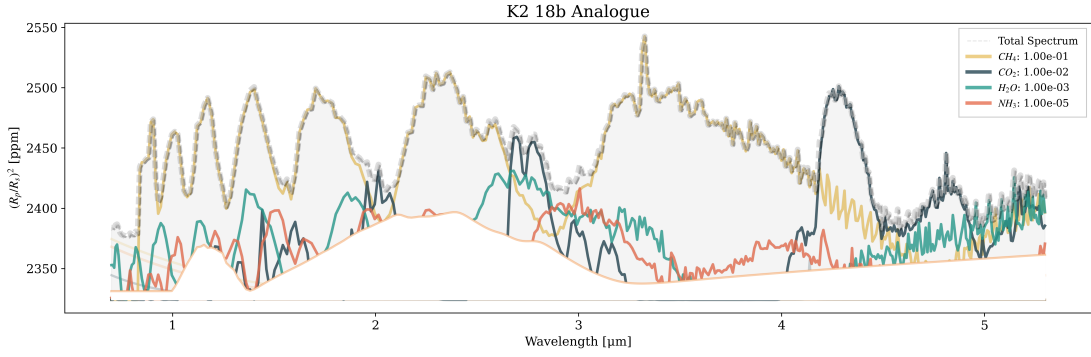


Fig. 9: Clean transmission spectrum of a *K2-18 b* analogue with an arbitrary (non-equilibrium) atmospheric composition. The contribution of each gas has been plotted as a continuous thick line, while the signal of the fill gases (H₂ and He, and their corresponding CIA) is shown as the white shaded curve below. The combined spectrum is limited by the dashed line and the shaded area in the background.

6.3. Stellar contamination

Since *K2-18* (the host star of our model case for sub-Neptunes) is a less active star than TRAPPIST-1 (the host star of our model case for terrestrial planets), we use a different set of stellar contamination parameters for training our algorithms. For the photospheric temperature, we use a fiducial value of $T_{\text{phot}} = 3500$ K, which is inside the range of temperatures estimated for *K218* (see Table 3). For the temperature of spots and faculae we use the ansatz in Rackham et al. (2018), namely $T_{\text{spot}} = 0.86 \times T_{\text{phot}}$ and $T_{\text{fac}} = T_{\text{phot}} + 100$ K. Finally, we use four equidistant values of the spot- f_{spot} and faculae- f_{fac} covering fractions between 0.0 and 0.3 which are systematically lower than those we used for TRAPPIST-1 (see Table 2).

6.4. The sub-Neptunes dataset

Using the previously chosen model parameters, the dataset for sub-Neptunes comprises 1058416 spectra = (66150 atmospheric compositions + 1 flat model) \times 16 contamination scenarios. Additionally, we augmented the database with 3 transit configurations (noise levels), namely one, two, and four total transits. For each transit configuration, we compute individually the corresponding instrumental noise. Technically, a fourth transit configuration, corresponding to a clean spectrum which can be regarded as an infinite number of transits, was also provided to the algorithm during the training phase.

The total volume of the dataset was 7793440 pairs of spectra (clean and contaminated), divided into 80% (~ 6.2 M) for model training and 20% (~ 1.5 M) for testing.

6.5. Model validation and evaluation

As we did in subsection 5.1 and Figure 5, to validate the performance of the sub-Neptunes G-DAE, we first performed a simple visual inspection of reconstructed spectra at different composition and contamination levels. Three examples of the results returned by the G-DAE trained in the sub-Neptunes dataset are shown in Figure 10.

A simple visual inspection, confirmed by the value of the χ^2 statistics, shows that the G-DAE is very successful at cleaning (top and bottom panels) and decontaminating (panel in the middle) sub-Neptune transmission spectra. This confirms that the power of G-DAE is not constrained to the particular chemical

composition, size, or stellar type we tested in our first numerical experiments.

A more in-depth, quantitative assessment of the algorithm's performance (model validation) on the test dataset yielded a validation MSE of 0.000534, an order of magnitude smaller than the corresponding metric in the terrestrial planet case (see subsection 4.3). This is explained by the significantly higher S/N of the spectra for larger planets. On the other hand, the test coefficient of determination in this case is $R^2 = 0.975$, which again is significantly better (in the scale of this particular metric) with respect to our first numerical experiment.

Lastly, we analysed the dependence of G-DAE performance on the number of transits (i.e., reducing the S/N). The results are presented, as we did in subsection 5.2 and Figure 6 for the terrestrial planet case, in Figure 11.

Independently of the fact that the conclusions in this case are very similar to the terrestrial planet G-DAE we discuss in subsection 4.3, namely, that the autoencoders are highly effective across a large range of noise and contamination levels, the dependence of χ^2 for the sub-Neptune G-DAE has striking similarities with the terrestrial planet one (see Figure 6) confirming that the behavior of the autoencoders is mostly independent of atmospheric model parameters and even signal strength.

7. Discussion and future directions

After designing and successfully testing our G-DAEs for the particular conditions of our experimental setup, several questions remain open. In this section, we assess the key concerns and caveats of our approach.

The first question that can be raised is whether, as is common in machine learning applications, the neural networks we trained are overly specific (overfitted) to the types of planets used in the training process. Therefore, we question whether this type of algorithm is sufficiently general to analyse real transmission spectra.

A key characteristic of our methods that makes them highly robust to overfitting is that, as explained in subsection 4.2 and subsection 6.4, our training datasets are highly diverse. Although the number of molecular species is relatively small, the mixing ratios span several orders of magnitude, yielding a large, heterogeneous set of spectra. On the other hand, planetary radius does not significantly affect the signals since G-DAE inputs and outputs are always normalized.

Comparison of spectra — 1 transit (Sub-Neptune)

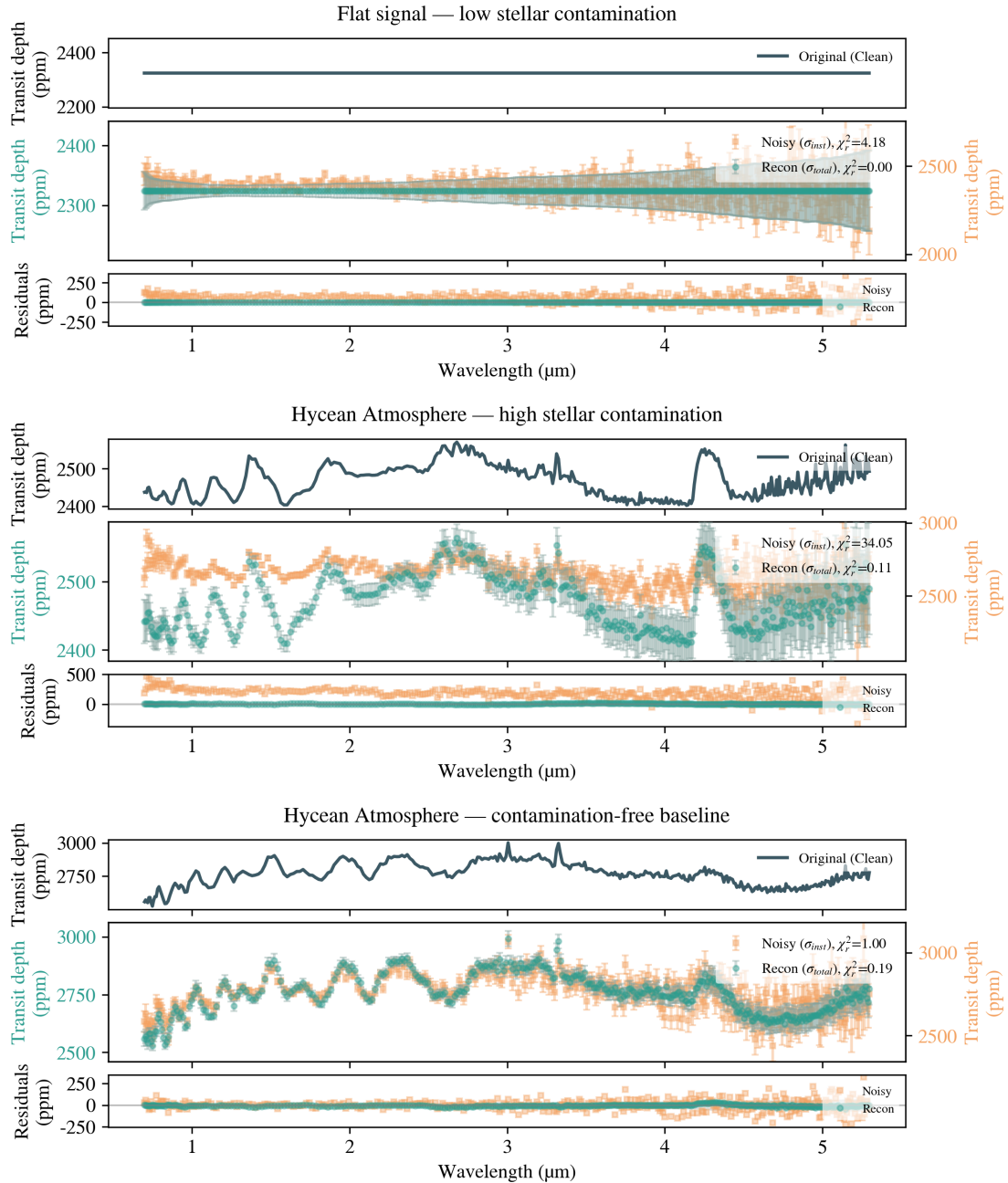


Fig. 10: Comparison between noisy and contaminated input spectra (square markers with error bars) and the reconstructions performed by our autoencoder networks (round markers) for a $K2-18 b$ analogue with different atmospheric compositions and stellar contamination, and when observed with JWST NIRSpec using a single transit. This figure is analogous to Figure 5.

The effect of stellar effective temperature T_{eff} is more complex. Assuming the same spot and faculae covering fractions, a cooler or hotter star will produce stellar contamination with different strengths and at different wavelengths. A G-DAE trained for a given T_{eff} could be “confused” when fed with a transmission spectrum of a star with a higher or lower temperature. We have tested the effect of stellar temperature and found that, over a range of a few hundred K, stellar contamination does not vary significantly with wavelength. As a result, the effect of, for instance, a slightly lower temperature will be interpreted by the algorithm as a slightly lower contamination.

If, on the other hand, the effective temperature of the true star is much higher than that used in the training dataset, the true contamination, due to astrophysical effects, could also be much lower; as a result, the G-DAE will reconstruct the data as if no contamination were present.

Still, more extensive experiments should be conducted to assess how the algorithms behave not only when stellar temperature varies but also when using different theoretical stellar spectral grids (see, e.g., Iyer et al. (2023); Husser et al. (2013)). What happens if the real spectrum has molecular species not included in the training dataset? Here, it is important to note that the au-

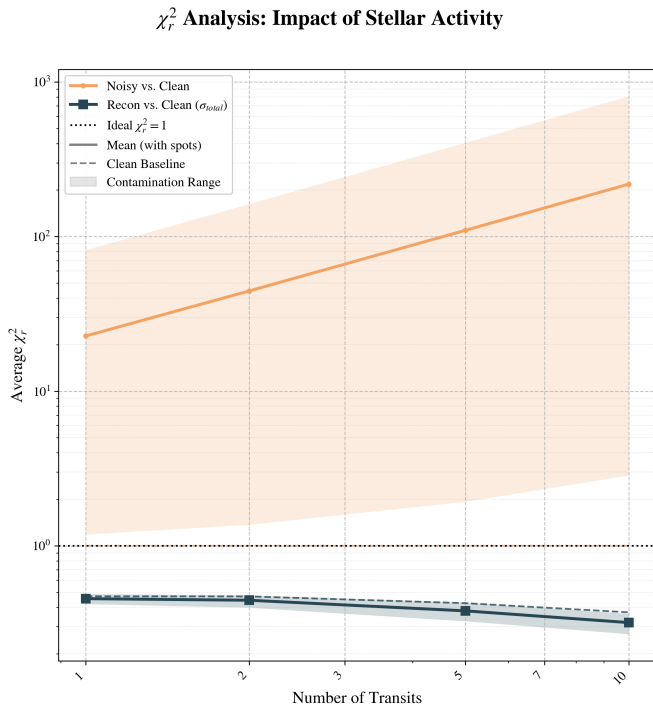


Fig. 11: Average reduced chi-square χ^2_r (continuous line) for G-DAE reconstructed spectra of sub-Neptune analogues as a function of number of transit (noise level). This figure is similar to Figure 6.

toencoder is trained to remove contamination, not to detect the signatures of molecular species. The G-DAEs are not intended to replace retrieval algorithms, which must deal with chemical diversity.

Still, if the algorithm detects significant spectral discrepancies between the actual and training datasets, this will not prevent the autoencoder from producing a best guess, but the “epistemic uncertainties” (see subsubsection 4.3.1) will be increased in the affected spectral region. The corresponding error bars will be passed to the retrieval algorithm, which should handle a slightly larger uncertainty. We have verified, however, that in most regions of the spectral range considered, epistemic uncertainties are much lower than instrumental uncertainties.

By design, the input and output signals of our G-DAE are normalized to the theoretical transit depth, i.e., to the radius of the planet found in literature. In real cases, the planetary radius is itself unknown and has its own uncertainties. Therefore, when using a production G-DAE, uncertainties in the normalization should be accounted for before performing the retrieval procedure. We have not evaluated the effect of these additional (although wavelength-independent) uncertainties on the test retrievals.

A possible caveat of the methodology is that, in real systems, stellar contamination may vary from one transit to the next.

We have focused on a single instrument, NIRSpec of JWST. It would be interesting to explore other instrumental setups or completely different telescopes and targets.

8. Summary and conclusions

Stellar contamination, or the transit light source effect, is one of the most limiting factors in transmission spectroscopy for exoplanets of all sizes. It affects especially exoplanets around active M-dwarfs (which are abundant and have yielded particularly interesting targets for astrobiological investigations), and its deleterious effects could be independent of signal strength (planetary size).

In this work, we present a novel neural-network-based methodology for decontaminating transmission spectra from noisy and/or contaminated signals. For that purpose we designed and optimized the architecture of the so-called general denoising autoencoders (G-DAE) a multi-layer mirror-structured neural network specialized at compressing/capturing the main features of a planetary transmission spectrum.

We trained two analogous but differently optimized G-DAE. One of them specialized in the transmission spectra of terrestrial planets with atmospheres of astrobiologically relevant compositions, and the other, in cleaning and decontaminating the signal of sub-Neptunes. For the first one, we trained the network using planetary analogues of *TRAPPIST-1 e*, and for the second one, we used the sub-Neptune *K2-18 b* as the model planet. Although trained with very specific planetary parameters, our results suggest that the performance of the G-DAEs is largely independent of stellar and planetary parameters.

A visual inspection of the reconstructed transmission spectra (see Figure 5 and Figure 10) shows that, almost irrespectively of noise and stellar contamination levels, neural networks perform impressively well. They learned the general features of theoretical spectra and applied their training to denoise realistic signals. A more thorough test, using different metrics and millions of synthesized noisy and contaminated spectra, confirms the conclusions.

The ability of autoencoders to clean transmission spectra could significantly improve the retrieval procedures (which is not the purpose of this work). As several experiments presented in this work have shown, the time of complex retrievals, including chemical and stellar contamination parameters, decreased by a factor of 3 to 6 when working with denoised spectra (see Figure 7). More importantly, in the case of significant contamination, working with reconstructed spectra seems to be the only reliable way to perform the retrieval process without incurring substantial errors (see Figure 8), at least when analysing the most interesting molecular species.

Finally, we have provided, along with the whole description of our methodology and the tests we performed, the numerical tools for immediate use of the G-DAEs we designed and tested for denoising actual transmission spectra obtained with JWST NIRSpec in the configuration chosen in this work.

Acknowledgements

A significant fraction of the results in this work were almost impossible to obtain in the span of a human life without the use of open-source Python packages, including (although not restricted to) `matplotlib` (Hunter 2007), `numpy` (Harris et al. 2020), `scipy` (Virtanen et al. 2020), `scikit-learn` (Pedregosa et al. 2011), `tensorflow` (Abadi et al. 2015), `TauReX` (Al-Refaei et al. 2021), `POSEIDON` (MacDonald 2023; Géron 2023), `mpi4py` (Dalcin & Fang 2021), `pandas` (McKinney 2010).

Data Availability

All data required to replicate the results and generate the figures presented in this work, including the Jupyter notebooks used to train and test the models, are available in the GitHub public repository <https://github.com/D4san/gdaespec>.

References

Abadi, M., Agarwal, A., Barham, P., et al. 2015, TensorFlow: Large-Scale Machine Learning on Heterogeneous Systems, software available from tensorflow.org

Al-Refaie, A. F., Changeat, Q., Waldmann, I. P., & Tinetti, G. 2021, The Astrophysical Journal, 917, 37

Bartlett, O. J., Benoit, D. M., Pimbblet, K. A., Simmons, B., & Hunt, L. 2023, Monthly Notices of the Royal Astronomical Society, 521, 6318

Benneke, B., Roy, P.-A., Coulombe, L.-P., et al. 2024, JWST Reveals CH\$_{4}\$S, CO\$_{2}\$S, and H\$_{2}\$O in a Metal-rich Miscible Atmosphere on a Two-Earth-Radius Exoplanet

Berahmand, K., Daneshfar, F., Salehi, E. S., Li, Y., & Xu, Y. 2024, Artificial Intelligence Review, 57, 28

Cadieux, C., Doyon, R., MacDonald, R. J., et al. 2024, The Astrophysical Journal Letters, 970, L2

Changeat, Q. & Yip, K. H. 2023, RAS Techniques and Instruments, 2, 45

Charbonneau, D., Brown, T. M., Noyes, R. W., & Gilliland, R. L. 2002, The Astrophysical Journal, 568, 377

Chollet, F. 2015, Keras, <https://github.com/fchollet/keras>

Chubb, K. L., Rocchetto, M., Yurchenko, S. N., et al. 2021, Astronomy & Astrophysics, 646, A21

Coulombe, L.-P., Benneke, B., Challener, R., et al. 2023, Nature, 620, 292

Dalcin, L. & Fang, Y.-L. L. 2021, Computing in Science & Engineering, 23, 47

Duque-Castaño, D. S., Zuluaga, J. I., & Flor-Torres, L. 2025, Monthly Notices of the Royal Astronomical Society, 539, 1528

Gal, Y. & Ghahramani, Z. 2016, Proceedings of The 33rd International Conference on Machine Learning, 48, 1050

Géron, A. 2023, Hands-on Machine Learning with Scikit-Learn, Keras, and TensorFlow: Concepts, Tools, and Techniques to Build Intelligent Systems, third edition edn. (Beijing Boston Farnham Sebastopol Tokyo: O'Reilly)

Gheller, C. & Vazza, F. 2021, Monthly Notices of the Royal Astronomical Society, 509, 990

Gordon, I., Rothman, L., Hargreaves, R., et al. 2022, Journal of Quantitative Spectroscopy and Radiative Transfer, 277, 107949

Guzmán-Mesa, A., Kitzmann, D., Mordasini, C., & Heng, K. 2022, Monthly Notices of the Royal Astronomical Society, 513, 4015

Harris, C. R., Millman, K. J., van der Walt, S. J., et al. 2020, Nature, 585, 357

Howard, A. W., Sinukoff, E., Blunt, S., et al. 2025, The Astrophysical Journal Supplement Series, 278, 52

Hu, R., Bello-Arufe, A., Tokadjian, A., et al. 2025, A Water-Rich Interior in the Temperate Sub-Neptune K2-18 b Revealed by JWST

Hu, R., Bello-Arufe, A., Zhang, M., et al. 2024, Nature, 1

Hunter, J. D. 2007, Computing in Science and Engineering, 9, 90

Husser, T.-O., Wende-von Berg, S., Dreizler, S., et al. 2013, Astronomy & Astrophysics, 553, A6

Iyer, A. R. & Line, M. R. 2020, The Astrophysical Journal, 889, 78

Iyer, A. R., Line, M. R., Muirhead, P. S., Fortney, J. J., & Gharib-Nezhad, E. 2023, The Astrophysical Journal, 944, 41

Jakobsen, P., Ferruit, P., Alves De Oliveira, C., et al. 2022, Astronomy & Astrophysics, 661, A80

Kaltenegger, L. & Traub, W. A. 2009, The Astrophysical Journal, 698, 519

Kendall, A. & Gal, Y. 2017, in Advances in Neural Information Processing Systems, Vol. 30 (Curran Associates, Inc.)

Kjærsgaard, R. D., Bello-Arufe, A., Rathcke, A. D., Buchhave, L. A., & Clemmensen, L. K. H. 2023, Astronomy & Astrophysics, 677, A120

Lim, O., Benneke, B., Doyon, R., et al. 2023, The Astrophysical Journal Letters, 955, L22

Liu, R., Lavvas, P., Tinetti, G., et al. 2025, Hydrocarbon Hazes on Temperate Sub-Neptune K2-18b Supported by Data from the James Webb Space Telescope

Lustig-Yaeger, J., Meadows, V. S., Crisp, D., Line, M. R., & Robinson, T. D. 2023, The Planetary Science Journal, 4, 170

Lustig-Yaeger, J., Meadows, V. S., & Lincowski, A. P. 2019, The Astronomical Journal, 158, 27

MacDonald, R. J. 2023, Journal of Open Source Software, 8, 4873

MacDonald, R. J. & Madhusudhan, N. 2017, Monthly Notices of the Royal Astronomical Society, 469, 1979

Madhusudhan, N. 2024, The Hycean Paradigm in the Search for Life Elsewhere

Madhusudhan, N., Constantinou, S., Holmberg, M., et al. 2025, The Astrophysical Journal Letters, 983, L40

Madhusudhan, N., Piette, A. A. A., & Constantinou, S. 2021, The Astrophysical Journal, 918, 1

Madhusudhan, N., Sarkar, S., Constantinou, S., et al. 2023, The Astrophysical Journal Letters, 956, L13

McKinney, W. 2010, in Proceedings of the 9th Python in Science Conference, 56–61

Melchior, P., Liang, Y., Hahn, C., & Goulding, A. 2023, The Astronomical Journal, 166, 74

Morvan, M., Nikolaou, N., Yip, K. H., & Waldmann, I. 2022, Don't Pay Attention to the Noise: Learning Self-supervised Representations of Light Curves with a Denoising Time Series Transformer

Niraula, P., de Wit, J., Gordon, I. E., Hargreaves, R. J., & Sousa-Silva, C. 2023, The Astrophysical Journal Letters, 950, L17

Niraula, P., de Wit, J., Gordon, I. E., et al. 2022, Nature Astronomy, 6, 1287

Parc, L., Bouchy, F., Venturini, J., Dorn, C., & Helled, R. 2024, Astronomy & Astrophysics, 688, A59

Pedregosa, F., Varoquaux, G., Gramfort, A., et al. 2011, Journal of Machine Learning Research, 12, 2825

Petit Dit De La Roche, D. J. M., Chakraborty, H., Lendl, M., et al. 2024, Astronomy & Astrophysics, 692, A83

Rackham, B., Espinoza, N., Apai, D., et al. 2017, The Astrophysical Journal, 834, 151

Rackham, B. V., Apai, D., & Giampapa, M. S. 2018, The Astrophysical Journal, 853, 122

Rackham, B. V., Apai, D., & Giampapa, M. S. 2019, The Astronomical Journal, 157, 96

Rackham, B. V. & De Wit, J. 2024, The Astronomical Journal, 168, 82

Rackham, B. V., Espinoza, N., Berdyugina, S. V., et al. 2023, RAS Techniques and Instruments, 2, 148

Rathcke, A. D., Buchhave, L. A., de Wit, J., et al. 2025, The Astrophysical Journal Letters, 979, L19

Rustamkulov, Z., Sing, D. K., Mukherjee, S., et al. 2023, Nature, 614, 659

Sarkar, S., Madhusudhan, N., Constantinou, S., & Holmberg, M. 2024, Monthly Notices of the Royal Astronomical Society, 531, 2731

Scorfield, M., Saintonge, A., de Mijolla, D., & Viti, S. 2023, Monthly Notices of the Royal Astronomical Society, 526, 3037

Sedaghat, N., Smart, B. M., Kalmbach, J. B., Howard, E. L., & Amindavar, H. 2023, Monthly Notices of the Royal Astronomical Society, 526, 1559

Snellen, I. A. G., De Kok, R. J., De Mooij, E. J. W., & Albrecht, S. 2010, Nature, 465, 1049

STScI. 2025a, NIRSpec Bright Object Time-Series Spectroscopy — JWST User Documentation, <https://jwst-docs.stsci.edu/jwst-near-infrared-spectrograph/nirspec-observing-modes/nirspec-bright-object-time-series-spectroscopy>, accessed: 2025-10-06

STScI. 2025b, NIRSpec Detector Subarrays — JWST User Documentation, <https://jwst-docs.stsci.edu/jwst-near-infrared-spectrograph/nirspec-detector-subarrays>, accessed: 2025-10-06

Swain, M. R., Vasisht, G., & Tinetti, G. 2008, Nature, 452, 329

Tennyson, J., Yurchenko, S. N., Al-Refaie, A. F., et al. 2016, Journal of Molecular Spectroscopy, 327, 73

Tinetti, G., Vidal-Madjar, A., Liang, M.-C., et al. 2007, Nature, 448, 163

Tsiaras, A., Waldmann, I. P., Tinetti, G., Tennyson, J., & Yurchenko, S. N. 2019, Nature Astronomy, 3, 1086

Virtanen, P., Gommers, R., Oliphant, T. E., et al. 2020, Nature Methods, 17, 261

Zhang, Z., Zhou, Y., Rackham, B. V., & Apai, D. 2018, The Astronomical Journal, 156, 178